Received: 13 April 2021 | Revised: 22 December 2021 | Accepted: 25 December 2021

DOI: 10.1002/nbm.4687

RESEARCH ARTICLE

NMR IN BIOMEDICINE WILEY

Methylated tetra-amide derivatives of paramagnetic complexes for magnetic resonance biosensing with both BIRDS and CEST

Abul B. M. Zakaria[1,2] | Yuegao Huang[1,2] | Daniel Coman[1,2] | Sandeep K. Mishra[1,2] | Jelena M. Mihailovic[1,2] | Samuel Maritim[1,2] | Federico A. Rojas-Quijano[3] | Paul Jurek[3] | Garry E. Kiefer[3] | Fahmeed Hyder[1,2,4]

[1]Department of Radiology and Biomedical Imaging, Yale University, New Haven, Connecticut, USA

[2]Magnetic Resonance Research Center, Yale University, New Haven, Connecticut, USA

[3]Macrocyclics, Dallas, Texas, USA

[4]Department of Biomedical Engineering, Yale University, New Haven, Connecticut, USA

Correspondence
Daniel Coman and Fahmeed Hyder, N143 TAC, 300 Cedar Street, Magnetic Resonance Research Center, Yale University, New Haven, CT 06510, USA.
Email: daniel.coman@yale.edu; fahmeed.hyder@yale.edu

Funding information
National Institutes of Health, Grant/Award Numbers: R01-EB023366, R01-CA140102

Paramagnetic agents that utilize two mechanisms to provide physiological information by magnetic resonance imaging (MRI) and magnetic resonance spectroscopic imaging (MRSI) are described. MRI with chemical exchange saturation transfer (CEST) takes advantage of the agent's exchangeable protons (e.g., -OH or -NH_x, where $2 \geq x \geq 1$) to create pH contrast. The agent's incorporation of non-exchangeable protons (e.g., -CH_y, where $3 \geq y \geq 1$) makes it possible to map tissue temperature and/or pH using an MRSI method called biosensor imaging of redundant deviation in shifts (BIRDS). Hybrid probes based upon 1,4,7,10-tetraazacyclododecane-1,4,7,10-tetraacetate chelate ($DOTA^{4-}$) and its methylated analog (1,4,7,10-tetraazacyclododecane-α, α′, α″, α‴-tetramethyl-1,4,7,10-tetraacetate, $DOTMA^{4-}$) were synthesized, and modified to create new tetra-amide chelates. Addition of several methyl groups per pendent arm of the symmetrical chelates, positioned proximally and distally to thulium ions (Tm^{3+}), gave rise to favorable BIRDS properties (i.e., high signal-to-noise ratio (SNR) from non-exchangeable methyl proton peaks) and CEST responsiveness (i.e., from amide exchangeable protons). Structures of the Tm^{3+} probes elucidate the influence of methyl group placement on sensor performance. An eight-coordinate geometry with high symmetry was observed for the complexes: **Tm-L1** was based on $DOTA^{4-}$, whereas **Tm-L2** and **Tm-L3** were based on $DOTMA^{4-}$, where the latter contained an additional carboxylate at the distal end of each arm. The distance of Tm^{3+} from terminal methyl carbons is a key determinant for sustaining BIRDS temperature sensitivity without compromising CEST pH contrast; however, water solubility was influenced by introduction of hydrophobic methyl groups and hydrophilic carboxylate. Combined BIRDS and CEST detection of **Tm-L2**, which features two high-SNR methyl peaks and a strong amide CEST peak, should enable simultaneous temperature and pH measurements for high-resolution molecular imaging in vivo.

Abbreviations: BIRDS, biosensor imaging of redundant deviation in shifts; CEST, chemical exchange saturation transfer; DIPEA, diisopropylethylamine; DMF, dimethylformamide; $DOTA^{4-}$, 1,4,7,10-tetraazacyclododecane-1,4,7,10-tetraacetate; $DOTMA^{4-}$, 1,4,7,10-tetraazacyclododecane-α, α′, α″, α‴-tetramethyl-1,4,7,10-tetraacetate; $DOTP^{8-}$, 1,4,7,10-tetraazacyclododecane-1,4,7,10-tetrakis(methylenephosphonate); FOV, field of view; HBTU, *O*-benzotriazole-*N*,*N*,*N*′,*N*′-tetramethyl-uronium-hexafluoro-phosphate; MRSI, magnetic resonance spectroscopic imaging; SAP, square antiprism; SNR, signal-to-noise ratio; TSAP, twisted square antiprism; UFF, Universal Force Field.

A.B.M. Zakaria, Yuegao Huang, Daniel Coman and Sandeep K. Mishra: these authors contributed equally to this work.

KEYWORDS
biosensing, methyl protons, molecular imaging, paramagnetic contrast agents, pH, temperature

1 | INTRODUCTION

MRI is an important non-invasive diagnostic tool in medicine because of its ability to produce high-resolution images of soft tissue, where image contrast is generated by relaxation times of water protons (i.e., longitudinal T_1 and/or transverse T_2). A critically important aspect for MRI advancement is using paramagnetic contrast agents to further enhance image contrast (e.g., by causing further T_1 reduction), resulting in greater delineation between normal and diseased tissues. The most successful class of MRI contrast agents is derived from gadolinium (Gd^{3+}) in combination with linear (open chain) or macrocyclic chelating agents.[1,2] These agents enhance image contrast by shortening the T_1 of water protons, but this enhancement is for the whole body due to non-specific distribution of chelated Gd^{3+} agents. For example, gadoteric acid or Dotarem (i.e., $GdDOTA^-$, where $DOTA^{4-}$ is an FDA-approved macrocyclic and is the abbreviation for 1,4,7,10-tetraazacyclododecane-1,4,7,10-tetraacetate), is used to distinguish lesions through T_1 enhancement, but it lacks specificity and fails to report on specific physiological events.

Alternatively, there is a growing interest in development of smart agents that are responsive to pathology.[3] Replacing Gd^{3+} in $GdDOTA^-$ with another lanthanide (Ln^{3+}) such as thulium (Tm^{3+}) gives rise to $TmDOTA^-$, which can measure temperature using its chemical shifts with MRSI.[4,5] Bansal and coworkers used MRI of the H5 proton of $TmDOTA^-$ with chemical shift selective gradient-echo images, but this could not provide absolute temperature readouts directly. However, MRSI can detect the protons on these agents directly to monitor the absolute temperature, opening a new avenue for molecular sensing.[6]

Smart agents are Ln^{3+} complexes with DOTA-based chelates. While paramagnetic hyperfine shifts of the endogenous proton resonances from the chelating ligands have been explored in classical NMR studies,[7] utilization of these shifted proton signals from the ligands as responsive agents has great potential in molecular imaging.[8] These Ln^{3+} complexes possess well resolved paramagnetically shifted proton resonances detected far beyond the diamagnetic range of proton NMR shifts,[9–14] and these non-exchangeable protons (e.g., $-CH_y$, where $3 \geq y \geq 1$) can be detected by high-speed MRSI to probe the microenvironment and this method is called biosensor imaging of redundant deviation in shifts (BIRDS).[6,15,16] These Ln^{3+} complexes can also contain exchangeable protons (e.g., -OH or $-NH_x$, where $2 \geq x \geq 1$) and/or bound water protons (exchange rates that are much slower than Gd-based T_1 agents[17]), where chemical exchange saturation transfer (CEST) can be used to generate MRI contrast from the same agent. MRI and MRSI experiments with CEST and BIRDS techniques, respectively, using a variety Ln^{3+} (e.g., thulium Tm^{3+}, europium Eu^{3+} or ytterbium Yb^{3+}) conjugated with various chelate designs is a rapidly growing area of research.[8,18–21] For example, $TmDOTP^{5-}$, which is Tm^{3+} complexed with 1,4,7,10-tetraazacyclododecane-1,4,7,10-tetrakis(methylenephosphonate) ($DOTP^{8-}$), has shown great potential for pH (and temperature) imaging in various pathological/disease states.[22–27]

Among lanthanide complexes for BIRDS, Tm^{3+} complexed with a methylated version of $DOTA^{4-}$ (i.e., $DOTMA^{4-}$, which is 1,4,7,10-tetraazacyclododecane-α, α′, α″, α‴-tetramethyl-1,4,7,10-tetraacetate) shows promise in temperature mapping because the hyperfine-shifted methyl proton resonance is ~100 ppm away from water proton resonance. These protons also have very short relaxation times (i.e., T_1 of 4.7 ms and T_2 of 4.2 ms), and have high temperature sensitivity (i.e., 0.7 ppm/°C at 35 °C).[6] More recently, Tm^{3+} and Yb^{3+} complexed with 1,4,7,10-tetraazacyclododecane-1,4,7,10-tetraaminophosphonate ($TmDOTA\text{-}4AmP^{5-}$ and $YbDOTA\text{-}4AmP^{5-}$) have been proposed as dual BIRDS and CEST modalities for pH and temperature imaging.[16] It should be noted, however, that dual BIRDS/CEST properties of probes such as $TmDOTA\text{-}4AmP^{5-}$ and/or $YbDOTA\text{-}4AmP^{5-}$ were discovered serendipitously, since the agents were commercially designed for only enhancing MRI contrast (i.e., T_1, T_2, or CEST). Regardless, using the chemical shift difference between proton resonances from $TmDOTA\text{-}4AmP^{5-}$ and $YbDOTA\text{-}4AmP^{5-}$, even higher pH and temperature sensitivities were obtained with BIRDS. In addition, pH values obtained from BIRDS were correlated with pH-sensitive CEST imaging. An important structural characteristic of these lanthanide complexes is that the non-exchangeable protons (for BIRDS) are positioned close to the paramagnetic metal ions (5-7 Å). Similarly, other work with Tm^{3+} and Eu^{3+} salts of 1,4,7,10-tetraazacyclododecane-1,4,7,10-tetraacetate tetraglycinate ($DOTA\text{-}(gly)_4^{4-}$) show that both $TmDOTA\text{-}(gly)_4^-$ and $EuDOTA\text{-}(gly)_4^-$ possess BIRDS and CEST properties.[15,28] Some novel work with Yb^{3+} complexes of a slightly modified $DOTP^{8-}$ chelate (i.e., 1,4,7-tris (methylenephosphonic acid)-10-(2-hydroxypropyl)-1,4,7,10-tetraazacyclododecane) develops unique pH sensitive CEST properties.[29] Moreover, for $EuDOTA\text{-}(gly)_4^-$, changing the oxidation state from +3 (when it is BIRDS/CEST active) to +2 enables this probe to generate both T_1 sensitivity and photoacoustic imaging.[30]

Inspired by high-temperature sensitivity of methyl protons in $TmDOTMA^-$ and dual BIRDS/CEST properties in agents such as $TmDOTA\text{-}4AmP^{5-}$ and $YbDOTA\text{-}4AmP^{5-}$ but also $TmDOTA\text{-}(gly)_4^-$ and $EuDOTA\text{-}(gly)_4^-$, we synthesized new tetra-amide probes composed of Tm^{3+} complexed with derivatives of $DOTA^{4-}$ and $DOTMA^{4-}$ containing several methyl groups per pendent arm (Figure 1). We embark on this task knowing

well that isomer formation is likely with so many methyl groups added. However, these probe designs and their comparisons could be considered novel given that there are no current paramagnetic agents with multiple methyl groups per pendent arm. Additionally, this experimental setup allowed us to test other hypotheses for designing new dual BIRDS/CEST agents. We hypothesized that methyl protons would provide both higher temperature sensitivities and redundancy for BIRDS, while exchangeable protons (i.e., amide groups) would provide opportunities for pH imaging with quantitative CEST. However, there were specific checks for dual BIRDS/CEST properties. We examined if placement of the methyl groups on the chelate (for BIRDS) alters the behavior of multiple exchangeable proton moieties (for CEST). For example, **Tm-L1** and **Tm-L2** were nearly identical tetra-amide structures, except that the latter had an additional methyl group. Another feature we wanted to examine was the properties of BIRDS versus CEST with regard to the probe's charge. For example, **Tm-L2** and **Tm-L3** were similar tetra-amide structures except that the latter had an additional carboxylate component, giving this chelate a negative charge. Additionally, comparison of **Tm-L2** with **Tm-L3** would allow us to understand if adding carboxylate groups improves solubility.

2 | EXPERIMENTAL

2.1 | Synthesis of the DOTA-tetraamide chelates

Structures and synthesis schemes of three methylated tetraamide derivatives (i.e., one DOTA-tetraamide derivative, **L1**, and two DOTMA-tetraamide derivatives, **L2** and **L3**, where the latter also has carboxylates) are shown in Figure 1.

2.1.1 | Tetrakis-(*N*-iso-propyl)-1,4,7,10-tetraazacyclododecane-1,4,7,10-tetracetamide-DOTA-(*i*-propyl-amide)$_4$ (L1)

The synthesis of **L1** follows the steps described previously.[31] Briefly, 2-bromo-*N*-isopropyl-acetamide was first synthesized by reacting iso-propylamine with 2-bromoacetylbromide in the presence of potassium carbonate. The resulting product was then added to the reaction mixture of cyclen (1,4,7,10-tetraazacyclododecane) and potassium carbonate in acetonitrile under N_2 to produce **L1**. ^{1}H NMR (500 MHz, D_2O;

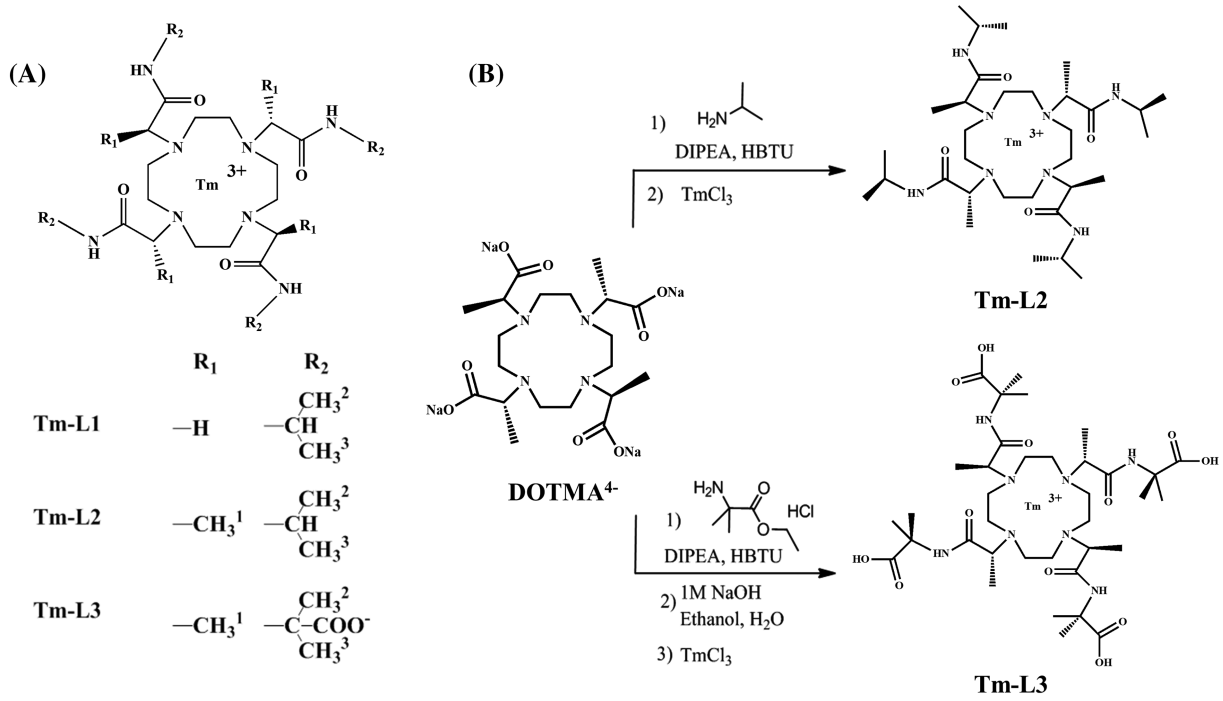

FIGURE 1 Structures and synthesis of Tm^{3+} complexes. A, Chemical structures of methylated TmDOTA-tetraamide derivative (**Tm-L1**) and TmDOTMA-tetraamide derivatives (**Tm-L2** and **Tm-L3**). B, Synthesis scheme of **Tm-L2** and **Tm-L3** complexes. See Figures S1 and S2 for characterization and purity for ligands and complexes

Figure S1a) δ (ppm) 3.34 (4H, p, CH), 3.05 (8H, s, CH_2) 2.28-2.68 (16H, m, CH), 1.19 (24H, d, CH_3); ^{13}C NMR (125 MHz, D_2O; Figure S1a) δ (ppm) 181.01, 59.63, 51.70, 44.36, 21.88.

2.1.2 | Tetrakis-(*N*-iso-propyl)-(1R,4R,7R,10R)-α,α′,α″,α‴-tetramethyl-1,4,7,10-tetraazacyclododecane-1,4,7,10-tetracetamide-DOTA-(*i*-propyl-amide)$_4$ (L2)

The synthesis of **L2** follows a similar scheme (Figure 1). DOTMA tetrasodium tetrahydrate salt (4.0 g, 6.6 mmol) was suspended in water (70 mL), and 6 M hydrochloric acid (6 mL, 36 mmol) was added while stirring. The resulting solution was evaporated under high vacuum to yield the hydrochloride salt of DOTMA as a white solid (5.3 g). The solids were suspended in dimethylformamide (DMF, 180 mL), and diisopropylethylamine (DIPEA) was added (13 mL, 75 mmol) with stirring. *O*-Benzotriazole-*N*,*N*,*N*′,*N*′-tetramethyl-uronium-hexafluoro-phosphate (HBTU) (12.5 g, 33 mmol) was added as a solid to the mixture and stirred for 5 min. After this, isopropylamine (3 mL, 35 mmol) was added to the reaction mixture and stirred at room temperature for 24 h. The solvent was removed by rotary evaporation under high vacuum and the residue was dissolved in chloroform (200 mL). The organic layer was washed five times with water (100 mL) and then dried over sodium sulfate. The product precipitated from solution at this point and was extracted from the drying agent by triturating in methanol (100 mL). The solvent was evaporated under reduced pressure to yield the product as a white solid (4 g, 97%). *m/z* (ESI-MS$^+$): 624.9 ([M + H]$^+$, 100%). ^{1}H NMR (500 MHz, D_2O; Figure S1b) δ (ppm) 3.72 (4H, td, CH), 3.20 (4H, q, CH), 2.81-3.86 (16H, m), 1.62 (12H, s, CH_3), 1.34 (24H, dd, CH_3). ^{13}C NMR (125 MHz, D_2O; Figure S1b) δ (ppm) 165.87, 58.37, 49.80, 47.98, 40.09, 37.82, 32.31, 23.24, 17.72.

2.1.3 | Tetrakis-(2-acetoamino-2-methyl-propionic acid)-(1R,4R,7R,10R)-α,α′,α″,α‴-tetramethyl-1,4,7,10-tetraazacyclododecane-1,4,7,10-tetracetamide-DOTA-(Me$_2$Gly)$_4$ (L3)

The synthesis of **L3** follows a similar scheme (Figure 1). DOTMA (6 g, 9.7 mmol) was suspended in water (100 mL), and 6 M HCl (8 mL, 48 mmoL) was added with stirring. The resulting solution was evaporated to dryness under high vacuum and the residue was suspended in DMF (100 mL). DIPEA (30 mL, 172 mmol) was added while stirring, followed by HBTU (16.6 g, 44 mmol). The mixture was stirred for 5 min and then 2-aminoisobutyric acid ethyl ester hydrochloride (7.8 g, 46.5 mmol) was added to the reaction mixture. The reaction was allowed to stir overnight at room temperature. The mixture was filtered through a medium-porosity sintered glass filter and the solvents were evaporated under high vacuum. The residue was dissolved in dichloromethane (50 mL) and washed three times with 1 M sodium hydroxide solution (50 mL). The organic layer was dried over sodium sulfate and filtered, and the filtrate was evaporated under reduced pressure. The residue was dissolved in a mixture of 1:1 ethanol/water (70 mL) and heated to 50 °C with stirring. Sodium hydroxide solution (50% wt) was added to the reaction mixture until the pH stabilized at 13. The solution was stirred at 50 °C for an additional 3 h then evaporated to dryness under high vacuum. The residue was dissolved in ethanol (30 mL) and the solution was stirred at room temperature for 3 d. The solids were filtered and washed with ethanol to yield the product as a white solid. *m/z* (ESI-MS$^+$): 800.94 ([M + H]$^+$, 100%). ^{1}H NMR (500 MHz, D_2O; Figure S1c) δ (ppm) 3.36 (4H, m, CH), 3.02-3.75 (16H, m, CH_2), 2.86-2.86 (24H, s, CH_3), 1.51 (12H, s, CH_3). ^{13}C NMR (125 MHz, D_2O; Figure S1c) δ (ppm) 177.50, 167.63, 165.87, 57.47, 54.02, 49.80, 38.92, 37.83, 32.31, 25.11.

2.2 | Preparation and characterization of thulium complexes

An aqueous solution of ligand (0.8 mmol) was stirred at ambient temperature and the pH adjusted to 7. Aliquots of $TmCl_3$ (0.5 M standard) were added while maintaining a constant pH = 7 via addition of NaOH (0.2 M) as required. Reaction progress was monitored using HPLC/MS. When complete conversion of ligand to complex was confirmed, the reaction mixture was filtered (0.22 μm) and the resulting filtrate lyophilized. The purity of complexes was above 90% by HPLC (Figure S2).

Tm(III)Tetrakis-(N-iso-propyl)-1,4,7,10-tetraazacyclododecane-1,4,7,10-tetracetamide-DOTA-(i-propyl-amide)$_4$ (**Tm-L1**). ^{1}H NMR (500 MHz, D_2O) δ (ppm) 43.13 (1H), 32.89 (1H), 22.04 (1H), 2.69 (2H), −9.06 (1H), −16.20 (1H), −25.91 (6H), −76.32 (1H), −87.62 (1H). *m/z* (ESMS EI+): 851 (100% [M + CF_3CO_2H]).

Tm(III)Tetrakis-(N-iso-propyl)-(1R,4R,7R,10R)-α,α′,α″,α‴-tetramethyl-1,4,7,10-tetraazacyclododecane-1,4,7,10-tetracetamide-DOTA-(i-propyl-amide)$_4$ (**Tm-L2**). ^{1}H NMR (500 MHz, D_2O) δ (ppm) 115.67 (3H), 88.06 (1H), 75.11 (1H), 63.97 (1H), −106.11 (3H), −267.23 (1H). *m/z* (ESMS EI+): 793 (M + H$^+$).

Tm(III) Tetrakis-(2-acetoamino-2-methyl-propionic acid)-(1R,4R,7R,10R)-α,α′,α″,α‴-tetramethyl-1,4,7,10-tetraazacyclododecane-1,4,7,10-tetracetamide-DOTA-(Me$_2$Gly)$_4$ (**Tm-L3**). ^{1}H NMR (500 MHz, D_2O) δ (ppm) 95.49 (3H), 88.42 (3H), 63.65 (1H), 44.89 (1H), 29.40 (1H), −11.94 (3H), −47.06 (1H), −100.09 (3H), −119.89 (3H). *m/z* (ESMS EI+): 967 (M + H$^+$).

2.3 | Crystallization and X-ray diffraction data collection

Uniform crystals for X-ray diffractions were grown over several days using a vapor diffusion method at room temperature. In this method, each complex with milligram quantities was placed in the individual vials and dissolved in the minimal volume (~0.5 mL) of acetonitrile. Then these vials were placed in the larger vials containing 5.0 mL of *n*-hexane.

Suitable crystals were mounted on glass fibers and the low-temperature diffraction data were collected on a Rigaku MicroMax-007HF diffractometer coupled to a Saturn 994 + CCD detector with Cu K_α ($\lambda = 1.54178$ Å) for the molecular structures. The diffraction images were processed and scaled using Rigaku Oxford Diffraction software (CrysAlisPro; Rigaku OD, The Woodlands, Texas). The structure was solved with SHELXT and was refined against F^2 on all data by full-matrix least squares with SHELXL.[32] All non-hydrogen atoms were refined anisotropically. Hydrogen atoms were included in the model at geometrically calculated positions and refined using a riding model. The isotropic displacement parameters of all hydrogen atoms were fixed to 1.2 times the *U* values of the atoms to which they are linked (1.5 times for methyl and water groups). The full numbering scheme of **Tm-L2** (007b-19,047) can be found in the full details of the X-ray structure determination (Crystallographic Information File, CIF), which is included in the Supporting Information (Tables S1-S7), where the CCDC number 2024208 (007b-19,047) contains the supplementary crystallographic data. The crystal structure of **Tm-L1** was unsolvable (007a-19,017, X-ray crystal data not shown) because it contained a few severely disordered water molecules and chloride ions. For **Tm-L1** and **Tm-L3**, a small single crystal was formed instead of a few large ones in several crystallization trials. Excessive nucleation could have happened due to the presence of unremovable anions (e.g., Cl^-, PF_6^-). These small crystals were insufficient for X-ray analysis. Thus, 3D models for **Tm-L1** and **Tm-L3** were built using IQmol and the 3D crystal structure of **Tm-L2** as input structure. Specifically for **Tm-L3** a carboxylic acid functional group was added to the four terminal carbons of the four pendent arms in **Tm-L2**. The initial structures of **Tm-L1** and **Tm-L3** were optimized to obtain a stable structure. The Universal Force Field (UFF)[33] has been used to optimize the geometry. The UFF can define almost all of the atoms in the periodic table. Because the structure contains a thulium (Tm^{3+}) metal ion, the UFF has been utilized to optimize the structure. After the geometry optimization, different structural parameters such as bond lengths and distances between different atoms were calculated. The calculated structural parameters for **Tm-L1** and **Tm-L3** were compared with that for **Tm-L2** (Table S1). Structural displays (3D) were produced using Mercury software (Version 4.3.1) available from Cambridge Crystallographic Database Centre. The chemical formulas for **Tm-L1**, **Tm-L2**, and **Tm-L3** based on integrating ^1H and ^{13}C NMR signals are $TmC_{28}H_{56}N_8O_4$, $TmC_{32}H_{64}N_8O_4$, and $TmC_{36}H_{56}N_8O_{12}$, respectively.

2.4 | Sample preparation for imaging experiments

A series of samples of **Tm-L1**, **Tm-L2**, and **Tm-L3** were prepared with 10 mM sodium phosphate buffer at various pH values (6.6-7.9) and 10% D_2O for BIRDS and PARACEST experiments. Sample pH values were measured using a pH meter (Mettler Toledo, Columbus, Ohio). All NMR experiments were acquired using an 11.7 T vertical magnet (Bruker, Billerica, Massachusetts).

2.5 | BIRDS characterization

The ^1H NMR chemical shifts for **Tm-L1**, **Tm-L2**, and **Tm-L3** samples (4 mM, pH ranges 6.6-7.9) were obtained by acquiring proton spectra at various temperatures (27 to 40 °C) and calibrated on a Bruker spectrometer (Billerica, MA) at 11.7 T as previously described[15]. All spectra were line broadened (20 Hz), phased, and baseline corrected. The chemical shifts of proton resonances were measured relative to the water resonance (0 ppm). Temperature sensitive methyl proton resonances in each complex were chosen for BIRDS detection. The temperature and pH dependences of proton chemical shifts were fitted to second-order polynomial equations:

$$\delta = a + b\ \mathrm{pH} + cT + d\,\mathrm{pH}^2 + eT^2 + f\,\mathrm{pH}\,T \tag{1}$$

where the coefficients *a*-*f* were obtained from the fit. The relaxation times (T_1 and T_2) of these resonances were measured at 35 °C using typical inversion-recovery and spin-echo methods, respectively.

2.6 | CEST characterization

All CEST experiments for **Tm-L1**, **Tm-L2**, and **Tm-L3** samples (4 mM, pH range 6.6-7.9) were collected with a continuous wave saturation RF pulse (53 μT, 4 s) over a range of frequencies (± 150 ppm, 0.5 ppm each step) followed by a short observe RF pulse to measure the residual water signal at different temperatures (25 to 40 °C) on a Bruker spectrometer at 11.7 T.[15] The CEST properties were analyzed by calculating the *Z* (or CEST)

spectra (i.e. plots of normalized bulk water signal intensity [M_s/M_0] as a function of saturation frequency). The CEST effect was quantified as a decrease in total bulk water intensity according to the following equation:

$$\text{CEST} = 1 - \frac{M_s}{M_0} \tag{2}$$

where M_s is the magnetization for saturation at the frequency of interest and M_0 is the reference magnetization for saturation at a frequency further away from resonance of interest.

The second term on the right-hand side of Equation 2 is inversely proportional to $(1 + kT_1)$, where k is the exchange rate and T_1 is the bulk water longitudinal relaxation time. k was determined by fitting the Z spectra to Bloch equations modified for chemical exchange.[34] The agent concentration (4 mM), the bulk water (90% H_2O or 49.5 M), the T_1 (1.9 ms for **Tm-L1**, 2.0 ms for **Tm-L2**, and 2.0 ms for **Tm-L3**), and the T_2 (0.8 ms for **Tm-L1**, 1.0 ms for **Tm-L2**, and 0.9 ms for **Tm-L3**) were considered fixed parameters, while the exchange rate constant k, the chemical shifts of the dilute pool and of bulk water, and the T_1 and T_2 for bulk water were obtained from the fit.

2.7 | In vitro BIRDS and CEST

The in vitro temperature maps with BIRDS and Z spectra with CEST were obtained in NMR tubes containing 4 mM of each agent on a Bruker spectrometer at 11.7 T as previously described.[15] The 3D MRSI datasets for BIRDS were obtained using a spectral window of 250 kHz, 1024 points, 389 spherical encoding steps, and 160 averages. The repetition time was TR = 6 ms and the encoding gradient duration was 160 μs. A 500 μs Shinnar-Le Roux (SLR) pulse was used for excitation of various proton resonances. The field of view (FOV) was 15 × 15 × 15 mm^3. The data were reconstructed to a 3D size of 15 × 15 × 15 to yield a voxel resolution of 1 × 1 × 1 mm^3. The temperature maps in each tube were calculated from the chemical shifts of methyl groups for each agent according to Equation 3. The CEST datasets were acquired using echo-planar imaging (EPI) with TR = 10 s, TE = 8 ms, FOV 20 × 20 mm^2, image size 40 × 40, slice thickness 2 mm, and 112 offsets in the range from −60 to 60 kHz.

3 | RESULTS AND DISCUSSION

3.1 | Design and synthesis

Three tetrasubstituted tetraaza-macrocyclic ligands were synthesized (Figure 1) and characterized (Figures S1-S2). The ligand L1 (i.e. a DOTA-tetramide derivative) was prepared by following the previously reported procedure, which involved the chemical conjugation of 2-bromo-*N*-isopropyl-acetamide with cyclen.[31] Subsequent acidification of the sodium salt form of $DOTMA^{4-}$ was used for both ligands L2 (ie a $DOTMA^-$tetramide derivative) and L3 (ie similar to L2 but with carboxylates). The ligand L2 was synthesized by reacting the protonated $DOTMA^{4-}$ with isopropylamine, while the ligand L3 was prepared by using the protonated $DOTMA^{4-}$ with 2-aminoisobutyric acid ethyl ester followed by hydrolysis of the ester bond. The identity and homogeneity of the three ligands were confirmed by ^1H NMR, chromatography, and mass spectroscopy. Tm^{3+} was chosen for complexation because it allows the most prominent hyperfine shifts for the non-exchangeable proton resonances.[35] The corresponding metal complexes were prepared by addition of stoichiometric amounts (1:1) of the ligand and the chloride salts of Tm^{3+} in aqueous solution at pH 7.0 (see Section 2 for details). The identity and homogeneity of thulium complexes was confirmed by NMR and mass spectroscopy. A xylenol orange assay was carried out to confirm complete metal complexation and ensure that there was no free detectable Tm^{3+}. The ^1H NMR spectra of the complexes showed no chemical shift drifting, loss of intensity, or line broadening after several years with similarly sharp proton resonances, demonstrating their great thermodynamic stability. Integration of ^1H and ^{13}C NMR peaks depicts the chemical formulas for **Tm-L1**, **Tm-L2**, and **Tm-L3** (Figure S1) in agreement with the high purity of the complexes (Figure S2).

Tm-L1 has two methyl groups in each pendent arm generating a single methyl ^1H peak (see $CH_3^{2,3}$ in Figure 2A). A modified **Tm-L1**, in which another methyl group was incorporated at position H6 of $TmDOTMA^-$, results in **Tm-L2** with an additional methyl ^1H peak (see CH_3^1 in Figure 2B). These three methyl groups are also present in **Tm-L3** but are shifted by the carboxylate and due to the twisted square antiprism (TSAP)/square antiprism (SAP) isomers there are several detectable methyl ^1H peaks (see CH_3^1 and $CH_3^{2,3}$ in Figure 2C). Regardless, these methyl ^1H peaks of **Tm-L3** show higher temperature sensitivities than those of $CH_3^{2,3}$ in **Tm-L1** (Table 1). All agents showed presence of amide proton signals (see -NH in Figure 2). The additional methyl proton resonance observed in **Tm-L2** and **Tm-L3** provides redundant information for BIRDS to report changes in the same molecular event (i.e., temperature) but with different sensitivities (Table 1).

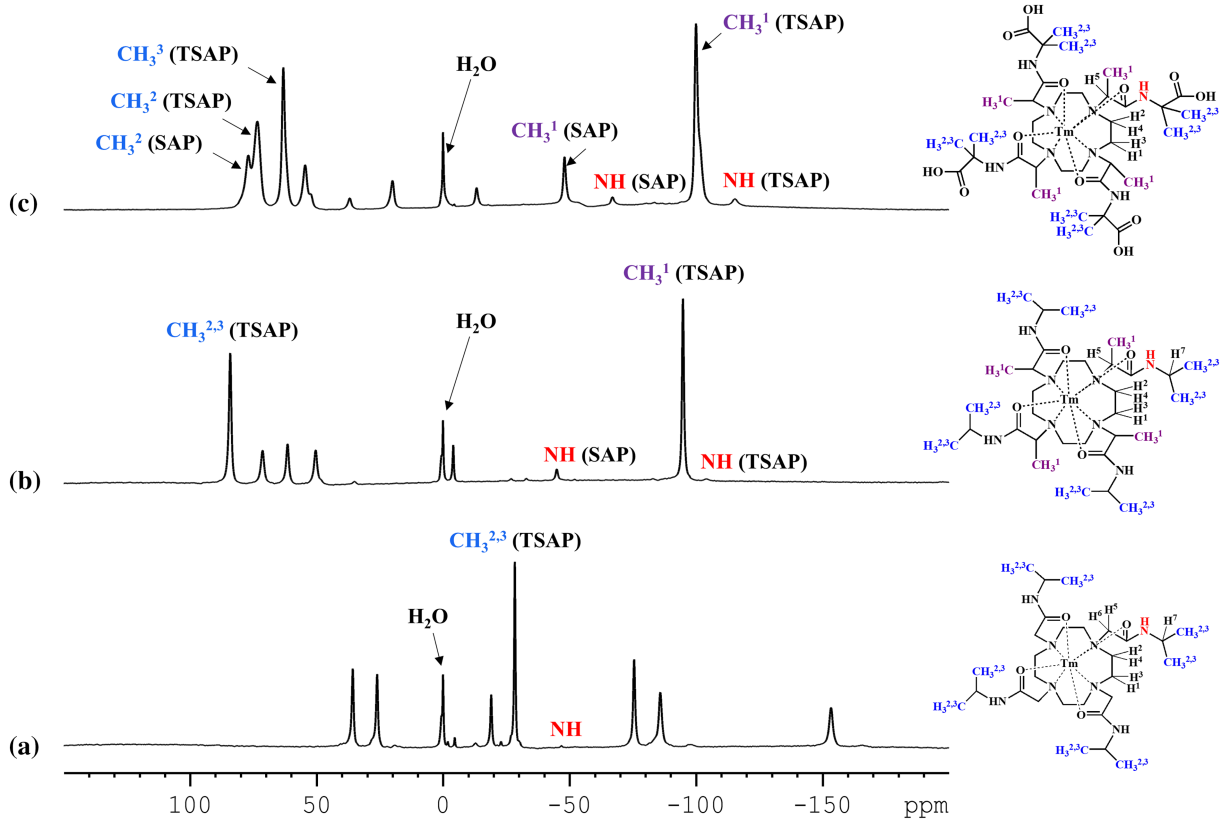

FIGURE 2 ^{1}H NMR spectra of 4 mM **Tm-L1** (A), **Tm-L2** (B), and **Tm-L3** (C) at pH 7.4 and 35 °C. Methyl protons are indicated with isomers as well as the -NH protons. See Figure S3 for all peak assignments. The H_2O peak in each spectrum is quite small because the majority of the water signal was suppressed by selective saturation with a block pulse for 100 ms. The amide NH protons are still visible, being in slow exchange with the bulk water, $k_{ex} < \delta_{NH} - \delta_{water}$, where k_{ex} is the exchange rate of the NH protons in s^{-1}, and δ_{NH} and δ_{water} are the Larmor frequencies in Hz of NH and water protons, respectively

TABLE 1 Properties of -CH_3 protons for **Tm-L1**, **Tm-L2**, and **Tm-L3** compared with $TmDOTMA^{-}$. See Supporting Information for further details on structures of **Tm-L1**, **Tm-L2**, and **Tm-L3** (Figures S3 and S4, Tables S1-S7). *from Reference 6; **from Reference 36

Complex	Specifics of -CH_3 protons	Chemical shift of -CH_3 protons (ppm)	Temperature sensitivity (ppm/°C)	Average Tm^{3+}-C (CH_3^x) distance (Å)	T_1 of -CH_3 protons (ms)	T_2 of -CH_3 protons (ms)	T_2/T_1
Tm-L1	$CH_3^{2,3}$	−28.6	0.183 ± 0.002	5.781	14.9 ± 0.6	6.3 ± 0.2	0.42
Tm-L2	CH_3^{1}	−96.2	0.373 ± 0.005	4.764	3.6 ± 0.2	3.1 ± 0.1	0.86
	$CH_3^{2,3}$	85.5	−0.372 ± 0.006	5.808	1.5 ± 0.1	1.2 ± 0.1	0.80
Tm-L3	CH_3^{1}	−99.6	0.607 ± 0.003	4.765	2.8 ± 0.1	1.7 ± 0.1	0.61
	CH_3^{2}	63.2	−1.31 ± 0.03	6.685	0.9 ± 0.1	0.7 ± 0.1	0.78
	CH_3^{3}	72.8	0.41 ± 0.01	5.310	1.5 ± 0.1	1.1 ± 0.1	0.73
Tm-L2	$CH_3^{2,3}$-CH_3^{1}		−0.74 ± 0.01		–	–	–
Tm-L3	CH_3^{2}-CH_3^{1}		−1.93 ± 0.03		–	–	–
	CH_3^{2}-CH_3^{3}		−1.72 ± 0.04		–	–	–
$TmDOTMA^{-*}$	CH_3	−99.2	0.7 ± 0.1	4.854**	4.7 ± 0.1	4.2 ± 0.2	0.89

3.2 | Structural properties of Tm^{3+} complexes

We defined the structural properties of the three Tm^{3+} complexes in solution together with the solid-state structure that are important for BIRDS (Tables S1-S7). We obtained the crystal structure for **Tm-L2** and 3D model-based structures for **Tm-L1** and **Tm-L3** (Figure 3; see Section 2.3 for

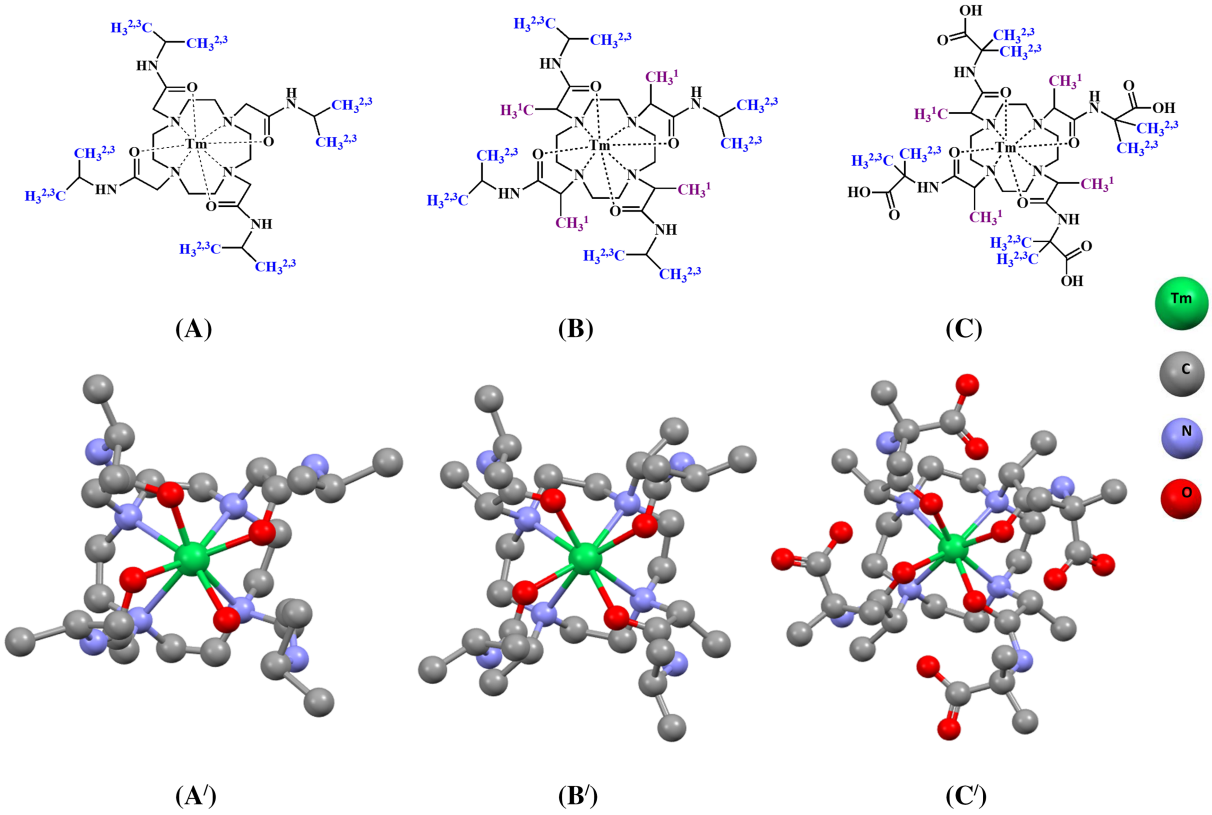

FIGURE 3 Molecular structures of **Tm-L1**, **Tm-L2**, and **Tm-L3** in 2D (A, B, and C) and 3D (A′, B′, and C′) models, where hydrogen atoms, solvent molecules, and counter-ions are omitted for clarity. The **Tm-L1** and **Tm-L3** structures were obtained from theoretical 3D modeling, while the **Tm-L2** structure was obtained from X-ray crystallography. See Table 1 and Supporting Information (Figures S4-S5, Tables S1-S7) for details

details). We also discuss the coordination geometry of Ln^{3+} complexes that are now well understood.[37,38] In DOTA-based symmetric complexes, the Ln^{3+} coordinates with the four nitrogen atoms on the cyclen (defines the N_4 plane) and the four oxygen atoms—one on each of the four pendent arms (defines the O_4 plane). Depending on the type of chelate and Ln^{3+}, an additional coordination position could be occupied by a bound water molecule capping the O_4 plane. Torsion of both N_4 and O_4 planes results in two possible cyclen ring conformations (δδδδ and λλλλ) and two pendent arm orientations (Δ and Λ). Thus, four diastereoisomers are possible, which are observed as two enantiomeric pairs. One enantiomeric pair is TSAP: Δδδδδ, Λλλλλ. Another enantiomeric pair is SAP: Λδδδδ, Δλλλλ. The abundance of TSAP and SAP forms is affected by both the Ln^{3+} and the chelate structure, where steric hindrance from the pendent arms increases TSAP abundance and SAP abundance depends on Ln^{3+} size. However, regulating the TSAP/SAP ratio in solution (at a given temperature) is important for applications of these DOTA-based symmetric complexes.

Two out of four stereoisomeric structures (TSAP, Λλλλλ, and SAP, Λδδδδ) are observed in the ^{1}H NMR spectrum of **α**-substituted DOTA derivatives such as LnTCE-DOTA,[38,39] LnNB-DOTA,[40] and LnDOTMA,[41] indicating that the other two (TSAP, Δδδδδ, and SAP, Δλλλλ) are unreachable due to unfavorable pendent arm rotation. In addition, the introduction of a substituent onto the pendent arms leads to preference for the TSAP coordination geometry.[42] Similar phenomena could be seen in **Tm-L1**, **Tm-L2**, and **Tm-L3**, where we observed TSAP form dominance at room temperature. However, the two favorable species TSAP (Λλλλλ) and SAP (Λδδδδ) are observed in ^{1}H NMR spectra of **Tm-L3** where TSAP exhibits a higher intensity than SAP (Figure S3), and under the same conditions **Tm-L1** and **Tm-L2** are comprised of the TSAP form primarily (Figure S3). From the crystal structure data, the N_4-O_4 torsion angle (α) of **Tm-L2** is 25.5°, while from the 3D optimized model of **Tm-L3** and **Tm-L1** they are 29.2°, and 20.5° respectively, consistent with reported results and demonstrating a relationship between coordination geometry and substitution of the pendent arms.

The structural information of the complexes shows eight coordination bonds, four for the nitrogen atoms of the cyclen ring and four for the oxygen atoms of the pendent arms, which demonstrates the high symmetry and rigidity of these complexes, resulting broadly in dispersed proton ($-CH_3^x$) resonances. The average distances between the central atom Tm^{3+} and the methyl carbon correlates with the temperature dependence of the chemical shifts. In **Tm-L1**, the average distance between Tm^{3+} and the carbons CH_3^2 and CH_3^3 is 5.78 Å, and the $CH_3^{2,3}$ proton resonance is closer to the bulk water signal compared with **Tm-L2** and **Tm-L3**, also demonstrating the lowest temperature sensitivity

(Tables 1 and S1). In contrast, the CH_3^x proton resonances of **Tm-L2** and **Tm-L3** complexes are more versatile. In **Tm-L2**, the average Tm^{3+}-C (CH_3^x) distances of two separate methyl carbon, CH_3^1 and $CH_3^{2,3}$, are 4.76 and 5.81 Å respectively (Table S1). In **Tm-L3**, the average distances of Tm^{3+}-C (CH_3^x) for the three separate methyl carbons, CH_3^1, CH_3^2, and CH_3^3, are 4.77, 6.69, and 5.31 Å respectively (Table S1). Among the three methyl protons, CH_3^2 shows the highest temperature sensitivity, potentially due to a steric effect and a hyperfine pseudocontact (through space), resulting from introducing CH_3^1 at the H6 (α) position and the carboxylic functional group on the terminal carbon, and the highest average distance from Tm^{3+}. Moreover, introducing a methyl group CH_3^1 at the H6 position makes a crucial difference in the coordination sphere among the **Tm-L2** and **Tm-L3** complexes. As a result, the average thulium-oxygen (Tm-O) pendent arm bond lengths for **Tm-L2** and **Tm-L3** are 2.271 and 2.289 Å, respectively, which are higher than that of 2.207 Å measured in **Tm-L1** (Table S1). This indicates that the methyl group on the H6 position elongated four Tm-O coordination bonds, resulting in the steric effect in entire complexation in **Tm-L2** and **Tm-L3** (Table S1). The phenomena are also reflected in the ^{1}H NMR of these complexes (Table 1, Figure 2). The chemical shift of $CH_3^{2,3}$ in the **Tm-L1** complex is closer to the water signal than for **Tm-L2** and **Tm-L3**. The average Tm-C ($CH_3^{2,3}$) distances for **Tm-L2** and **Tm-L3** are 4.99 and 5.22 Å, respectively, which are higher than the 4.88 Å for **Tm-L1** (Table S1). Moreover, the average M-CH_3^2 and M-CH_3^3 distances for **Tm-L2** are ≥6.43 and ≥5.19 Å, respectively, while those for **Tm-L3** are ≥6.69 and ≥5.31 Å, respectively. These are higher than the 6.51 and 5.05 Å measured for **Tm-L1** (Table S1). Interestingly, the longer distances of Tm-C ($CH_3^{2,3}$) in **Tm-L2** and **Tm-L3** blended with the steric effect of CH_3^1 contribute to deshielding of the terminal protons, resulting in higher chemical shifts. However, introducing the carboxylic group on the terminal carbon in **Tm-L3** disturbs the combined resonance of $CH_3^{2,3}$, resulting in two distinct well resolved resonances for CH_3^2 and CH_3^3 (Table 1, Figure 2).

3.3 | NMR spectroscopy

^{1}H NMR spectra of all three Tm^{3+} complexes demonstrate sharp paramagnetically shifted proton resonances. The hyperfine-shifted proton resonances of the Tm^{3+} complexes span a range from −160 to 90 ppm with linewidths of 50-450 Hz in 10% deuterium oxide (Figure 2). ^{1}H spectra of the **Tm-L1** complex show seven non-exchangeable proton resonances, six of which have the same integrated intensities while one demonstrated a sixfold higher intensity corresponding to the two methyl groups at the terminus of each pendent arm at −28.6 ppm (Figure 2A). The **Tm-L2** complex has six non-exchangeable proton resonances, two of which have higher intensities corresponding to the dimethyl protons of $CH_3^{2,3}$ resonating at 85.5 ppm, while the methyl protons of CH_3^1 resonate at a chemical shift of −96.2 ppm (Figure 2B). This is similar to the **Tm-L3** complex, where the dimethyl protons resonate slightly apart from each other (i.e., at 63.2 and 72.8 ppm), while the single methyl protons resonate at −99.6 ppm (Figure 2C). This effect could be due to the charged pendent arm of Tm-L3, which segregates methyl group ($CH_3^{2,3}$) having different orientations.

The relaxation times (T_1, ms) and chemical shifts of methyl protons are correlated well with crystal structures, and are consistent with the literature reported,[42,43] supporting the assignments of proton resonances. In **Tm-L1** (Figure 3A), the most remote C-H (dimethyl proton, average Tm-CH_3^2 and Tm-CH_3^3 distance of 5.78 Å) demonstrates the smallest chemical shift at −28.6 ppm and the longest T_1 value ($T_1 = 14.9 \pm 0.6$ ms) (Figure S4). The assignment of the methyl proton (-CH_3) of $TmDOTMA^-$ is also consistent with that of **Tm-L2** in terms of the highest T_1 value with a similar distance of Tm-CH_3^1 (see Table 1, but additional details can be found in Figure S5 and Table S1). For **Tm-L2** (Figure 3B), the single methyl proton (CH_3^1, average Tm-CH_3^1 distance of 4.76 Å) shows a higher T_1 value (3.60 ± 0.2 ms) compared with the dimethyl proton ($CH_3^{2,3}$, average Tm-CH_3^2 and Tm-CH_3^3 distance of 5.81 Å), with $T_1 = 1.5 \pm 0.1$ ms. For **Tm-L3**, the results indicate a consistency with the values measured for **Tm-L2** and $TmDOTMA^-$. In this case, the highest shifted single methyl (CH_3^1) resonance at −99.6 ppm has similar Tm-CH_3^1 distance of 4.76 Å and the longest T_1 (2.8 ± 0.1 ms), comparable to that of $TmDOTMA^-$. In addition, **Tm-L3** has the smallest T_1 value (0.9 ± 0.1 ms), with chemical shift at 63.2 ppm (Figure 3C, Table 1, Figure S4). In agreement with our hypothesis for **Tm-L1**, **Tm-L2**, and **Tm-L3** (see Section 1), all methyl protons have very short relaxation times because of dipolar interactions at the level of 5-7 Å (Table S1) between the non-exchangeable protons and the unpaired Tm^{3+} electrons. Overall, the T_1 value of methyl protons is higher in **Tm-L1** than in **Tm-L2** and **Tm-L3** because of potential rotational freedom restrictions caused by the presence of four additional methyl groups in the **Tm-L2** and **Tm-L3**. Similarly, the T_1 values of $CH_3^{2,3}$ in **Tm-L2** and **Tm-L3** are smaller than that of CH_3^1 in the same complex.

Prediction of chemical shifts of methyl protons in these Tm^{3+} complexes is difficult because of competing effects of electronic shielding, orientation relative to local B_0 field, and orientation and proximity to the Tm^{3+} ion.[44,45] Bansal and colleagues[35] demonstrated that the hyperfine shifts of a single methyl proton group in $DOTMA^{4-}$ can be dramatically switched on opposite sides of the water peak when different Ln^{3+} ions are used for complexation. Chemical shifts of methyl protons were assigned by comparing with the methyl proton resonance of $TmDOTMA^-$.[6,35] $TmDOTMA^-$ has a methyl group in position R1 (Figure S4), which resonates upfield of water (negative chemical shifts), similar to **Tm-L2** and **Tm-L3**. Note that **Tm-L1** does not have a methyl group in position R1, whereas all ligands have methyl groups in position R2. Based on this observation we assigned the negative chemical shifts observed in **Tm-L2** and **Tm-L3** to the CH_3^1 groups (similar to $TmDOTMA^-$). The CH_3^2 and CH_3^3 resonance assignments were made by choosing the highest MR signals from the remaining unassigned resonances in each spectrum, since the methyl groups produce higher signals due to a larger number of non-exchangeable protons.

3.4 | BIRDS characterization

BIRDS is an ultra-high-speed 3D MRSI method, which has several advantages over conventional techniques, including higher sensitivities to molecular events, overlap-free ^{1}H hyperfine shifts, and favorable relaxation properties (short T_1 and T_2) for detection.[46] Molecular imaging with BIRDS using paramagnetic complexes relies on their superior sensitivities to changes induced by molecular events (e.g., pH and temperature). Thus, improved molecular sensitivity is a key factor when designing contrast agents for BIRDS imaging. For example, TmDOTMA$^-$ is an excellent probe for temperature mapping using the chemical shift of its methyl protons.[6,35] The methyl proton resonance of TmDOTMA$^-$ has a temperature sensitivity of 0.7 ppm/°C and T_2/T_1 ratio of 0.88.[6] The four methyl groups on the pendent arms of TmDOTMA$^-$ are chemically equivalent. For each molecular agent, due to the C2 symmetry of the molecule, 12 molar methyl protons contribute to the same chemical shift resonance. As much as a fivefold increase in signal-to-noise ratio (SNR) was observed compared with TmDOTP^{5-}, due to four methyl groups replacing four ^{1}H atoms (at the H6 position) and thus providing 12 magnetically equivalent protons. The measured fivefold increase in SNR is due to a threefold increase in the number of contributing protons, but also because the resonance has a smaller linewidth due to its shorter correlation time. Similar results were suggested by Parker et al when a *tert*-butyl group was added to one pendent arm of the macrocyclic complexes to increase the redundancy, achieving increased SNR and higher sensitivity.[47]

The temperature and pH dependences for the chemical shifts of methyl protons in **Tm-L1**, **Tm-L2**, and **Tm-L3** were characterized in the range of 25-40 °C and pH 6.6-7.9, and are plotted in Figure S6. The coefficients *a*-*f* determined from the fit using Equation 1 are shown in Table S8. For methyl protons in **Tm-L1**, **Tm-L2**, and **Tm-L3**, absolute temperature sensitivities varied from 0.183 to 1.31 ppm/°C (Table 1, top three rows). The methyl proton in **Tm-L1** was less temperature sensitive than the methyl protons in **Tm-L2** and **Tm-L3**. The dimethyl protons in **Tm-L2** showed almost the same temperature sensitivities (i.e., 0.373 and −0.372 ppm/°C) but with opposite signs. The largest temperature sensitivity was observed for CH_3^2 in **Tm-L3** (i.e., −1.31 ppm/°C), while those for CH_3^1 and CH_3^3 were lower (0.607 ppm/°C and 0.41 ppm/°C, respectively). The T_1 and T_2 values for methyl protons in each Tm^{3+} complex was measured to estimate the T_2/T_1 ratio, which is an important factor determining the SNR. The T_1 and T_2 for $CH_3^{2,3}$ in **Tm-L1** were larger than those for methyl protons in **Tm-L2** and **Tm-L3**. Methyl protons in **Tm-L2** exhibited an optimal T_2/T_1 ratio (close to 1), whereas the methyl proton in **Tm-L1** had a less favorable T_2/T_1 ratio (0.42).

Since the chemical shifts of methyl protons in the three Tm^{3+} complexes investigated are pH insensitive (Figure 4), these complexes are good BIRDS probes for absolute temperature measurements. Thus, for temperature calibration of each methyl proton, the absolute temperature (T) was calculated using the change in the chemical shift δ_x according to

$$T = A + B(\delta_x - \delta_0) + C(\delta_x - \delta_0)^2 \tag{3}$$

where δ_0 was set to the mean of the chemical shifts measured in the temperature range investigated, and the coefficients A, B, and C were determined from a linear least-square fit of the measured temperature as a function of the chemical shift. The δ_0 and the coefficients A, B, and C for each chemical shift (or for the chemical shift difference between two methyl protons) are summarized in Table 2. For dimethyl protons investigated in **Tm-L2** and **Tm-L3**, absolute temperature sensitivities increased dramatically from −0.74 to −1.93 ppm/°C, comparing well with TmDOTMA$^-$ (with a single methyl group), which has a temperature sensitivity of 0.7 ppm/°C (Table 1, bottom three rows). The comparative sensitivities of the individual methyl protons of **Tm-L1** and the dimethyl protons of **Tm-L2** and **Tm-L3** are shown in Figure 4 and Figure S6.

As suggested by results in our and other laboratories, using chemical shift difference between two resonances is very helpful for BIRDS imaging.[5,16] In both **Tm-L2** and **Tm-L3**, multiple methyl proton resonances are observed at different chemical shifts and are differently affected by the same molecular event (i.e., temperature).[5,48] For example, CH_3^1 and $CH_3^{2,3}$ in **Tm-L2** show almost the same absolute temperature sensitivities but with opposite signs; thus, the chemical shift difference between these two resonances shows a sensitivity of 0.74 ppm/°C (Table 1). Higher temperature sensitivities were observed using the chemical shift differences between methyl proton resonances in **Tm-L3** (temperature sensitivities for CH_3^2-CH_3^1 and CH_3^2-CH_3^3 are −1.93 ppm/°C and −1.72 ppm/°C, respectively; see Table 1, bottom three rows). To our knowledge, **Tm-L3** provides the highest temperature sensitivity so far amongst all known BIRDS agents. Another advantage of using the chemical shift difference between two proton resonances arising from the same agent is to circumvent the errors generated by B_0 field inhomogeneity or susceptibility differences that might affect the chemical shift of the water resonance often used as a reference.[5,48] Furthermore, similar to the methyl proton resonances in TmDOTMA$^-$, the chemical shifts of methyl proton resonances of the three Tm^{3+} complexes investigated here are not sensitive to pH (Figure 4). The pH independence of these agents simplifies the temperature determination with BIRDS.

The introduction of methyl groups yields neutral ligands L1 and L2; however, **Tm-L1** and **Tm-L2** are cationic species, though their water solubility decreases due to the long uncharged arms and hydrophobic cyclen ring. While the hydrophobic feature of these molecules might lower their translational potential, approaches that allow incorporation of these agents within nanospheres (e.g., micelle and liposome) and/or coating them with nanostructures would help their delivery to the targeted site.[49] We anticipate that encapsulation of **Tm-L2** inside liposomes would increase local concentration, while chemical shifts would not be affected, as previously shown.[50]

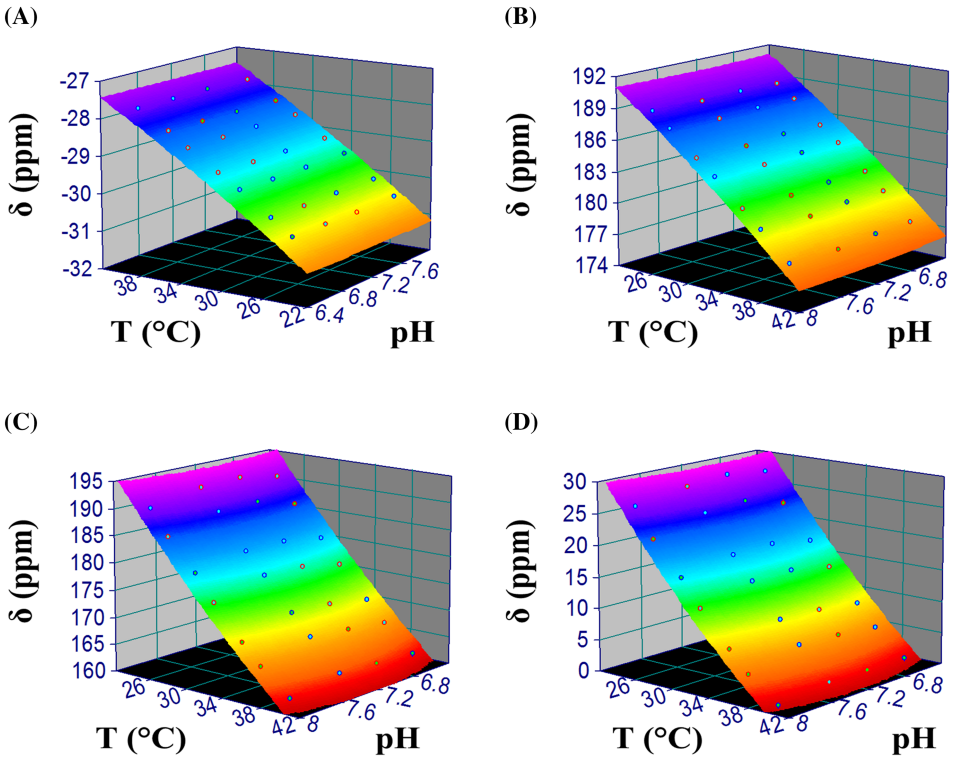

FIGURE 4 Temperature and pH dependences of chemical shifts for $CH_3^{2,3}$ of **Tm-L1** (A) and chemical shift differences between protons $CH_3^{2,3}$ and CH_3^{1} of **Tm-L2** (B), CH_3^{2} and CH_3^{1} of **Tm-L3** (C) and CH_3^{3} and CH_3^{2} of **Tm-L3** (D). See Supporting Information (Figure S6, Table S8) for details

3.5 | CEST characterization

The Tm^{3+} complexes were designed to include exchangeable protons on the pendent arms so that they can be used for CEST imaging. The temperature and pH dependences of the CEST effect were investigated for each complex (Figure 5). While only a small CEST effect was detected for **Tm-L3**, a much larger CEST effect was observed for exchangeable pools in **Tm-L1** and **Tm-L2**. In contrast to BIRDS properties, the CEST effect in these complexes was responsive to both temperature and pH. A larger CEST effect was observed at higher temperature and pH values. Temperature and pH effects in CEST were largest in **Tm-L1** and smallest in **Tm-L3**. The offsets of the CEST profiles were shifted towards the water resonance upon increasing temperature, while the offsets of the CEST profiles were not shifted when pH was changed, indicating that the exchange rates are pH dependent as expected, while the structures of these complexes were not affected by pH changes in this range. The temperature sensitivities for the CEST peaks in **Tm-L1**, **Tm-L2**, and **Tm-L3** were 0.60 ± 0.01, 0.47 ± 0.01, and 0.34 ± 0.02 ppm/°C, respectively. However, the pH sensitivities for the chemical shifts of CEST peaks in **Tm-L1**, **Tm-L2**, and **Tm-L3** were not significant (i.e., less than 0.01 ppm/pH unit). Therefore, these three Tm^{3+} complexes can also be used for pH imaging with CEST, where the temperature could be measured with BIRDS.[16]

The strong pH dependence of CEST peak heights suggests that these exchangeable peaks are probably amide peaks. We calculated their rate constants (9925 s^{-1} for **Tm-L1**; 7815 s^{-1} for **Tm-L2**; 864 s^{-1} for **Tm-L3**) using Bloch equations modified for chemical exchange.[34] Because most of the previously published exchange rate constants were measured in non-Tm-based agents, we compare our measurements with those of Eu-based agents, such as EuDOTA-$(gly)^-$ 19 000 s^{-1}, EuDOTA-$(AmPO_2OBu)^-$ 14 085 s^{-1}, EuDOTA-(glyOEt) 10 000 s^{-1}, and EuDOTA-$(Me_2gly)^-$ 35 714 s^{-1}.[31,51–55] However, exchange rate constants for **Tm-L2** and **Tm-L3** are closer to those for TmDOTA-$(gly)_4^-$ (i.e., 1703 s^{-1}).[28] This comparison indicates that the three Tm^{3+} complexes investigated here have slower exchange rate constants. We hypothesized that the main sources for CEST peaks in these agents will be amide protons and/or bound water. Previous work with DOTA-$(gly)^{4-}$[15,28] has shown that EuDOTA-$(gly)^-$ possesses both amide proton and bound water signals (the latter and former at +60 ppm and −5 ppm, respectively), whereas TmDOTA-$(gly)^-$ has only the amide proton signal (at −60 ppm). Based on the exchange rates estimated for a range of CEST agents (see above) and the fact that no bound water signal was visualized at the lower temperature of 10 °C, we conclude that the CEST peaks are all of amide origin, where **Tm-L3** has additional smaller peaks arising from the SAP isomer, and this is much less in **Tm-L2** (Figure 5).

Lanthanide-based cyclen agents have attracted attention for CEST applications, for measuring changes in various molecular events, such as pH,[16,56] temperature,[15,57] metabolites,[58,59] or metal ions.[60] The main advantage of CEST with paramagnetic agents is the larger offset differences between the exchangeable pools and the bulk water resonance.[10,61] The CEST effect is generally observable when the exchange rate is not larger

TABLE 2 Coefficients *A*, *B*, *C*, and δ_0 for temperature determination using the methyl resonances with Equation 3

	$CH_3^{2,3}$ (Tm-L1)	CH_3^{1} (Tm-L2)	$CH_3^{2,3}$ (Tm-L2)	$CH_3^{2,3}$-CH_3^{1} (Tm-L2)	CH_3^{1} (Tm-L3)	CH_3^{2} (Tm-L3)	CH_3^{3} (Tm-L3)	CH_3^{2}-CH_3^{1} (Tm-L3)	CH_3^{2}-CH_3^{3} (Tm-L3)
A	32.11 ± 0.01	32.43 ± 0.01	32.49 ± 0.01	32.47 ± 0.01	32.22 ± 0.03	31.99 ± 0.08	31.84 ± 0.02	32.06 ± 0.06	31.95 ± 0.06
B	5.41 ± 0.01	2.673 ± 0.003	−2.67 ± 0.01	−1.336 ± 0.001	1.65 ± 0.01	−0.74 ± 0.01	2.37 ± 0.01	−0.512 ± 0.004	−0.566 ± 0.004
C	0.21 ± 0.001	−0.042 ± 0.002	−0.059 ± 0.003	−0.013 ± 0.001	−0.007 ± 0.002	0.007 ± 0.001	0.098 ± 0.004	0.0024 ± 0.0004	0.0043 ± 0.0006
δ_0	−29.163	−97.155	86.443	183.598	−100.911	76.014	62.009	176.925	14.005

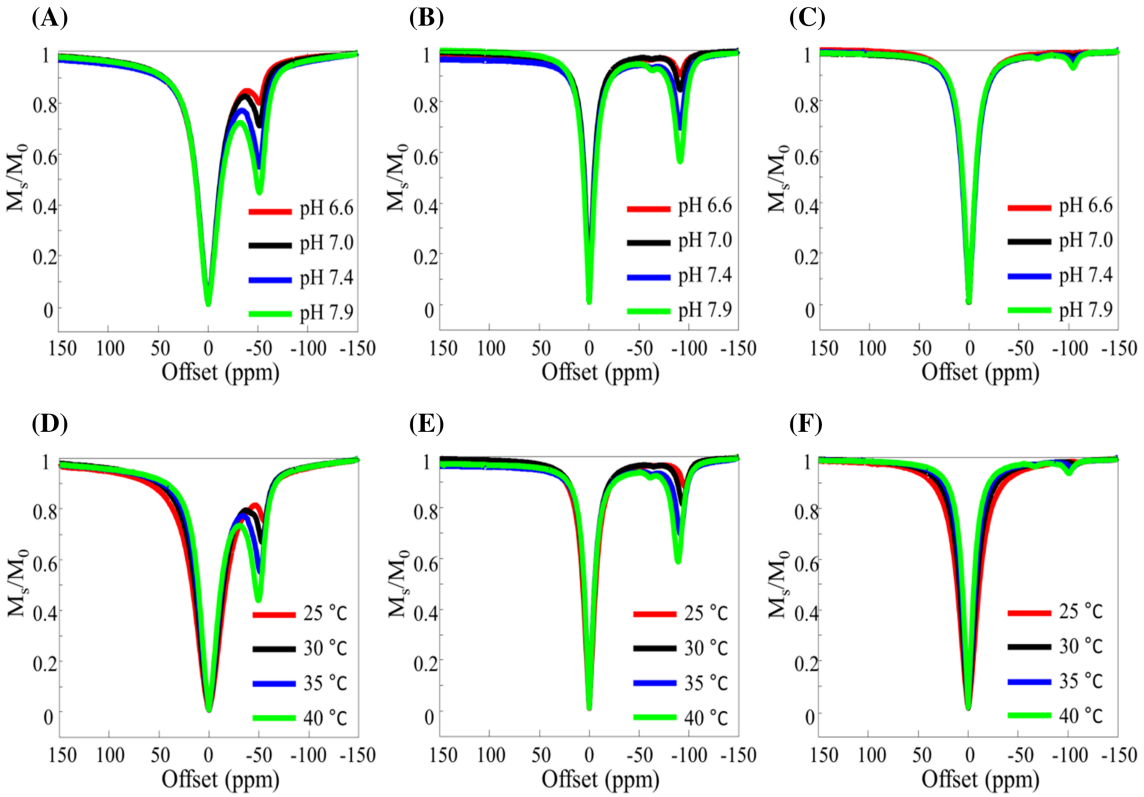

FIGURE 5 pH dependences of CEST spectra of 4 mM **Tm-L1** (A), **Tm-L2** (B), and **Tm-L3** (C) at 35 °C, and temperature dependences of CEST spectra of 4 mM **Tm-L1** (D), **Tm-L2** (E), and **Tm-L3** (F) at pH 7.4 using a B_1 value of 53 μT for 4 s. The amide proton exchange rate constants calculated using Bloch equations modified for chemical exchange were 9925 s^{-1} for **Tm-L1**, 7815 s^{-1} for **Tm-L2**, and 864 s^{-1} for **Tm-L3**

than the chemical shift difference between the two pools. Unfortunately, no CEST effect is detected for $TmDOTA^-$ and $TmDOTMA^-$ at physiological conditions, probably because the exchange of the bound water in these agents is too fast. Thus, $TmDOTMA^-$ is mainly used for temperature measurements in BIRDS, although it could be used as a shifting agent to generate a CEST effect when it is encapsulated inside the liposome.[62]

Note that the CEST effect in **Tm-L1** and **Tm-L2** is much larger than that in **Tm-L3**, possibly due to the hydrophobicity of the structures. The enhanced hydrophobicity could be responsible for repelling the free water molecules, thus slowing down the exchange to bring the exchange rate into an optimal regime for enhanced CEST effect.[31] These probes still have great potential in translational temperature and/or pH imaging if they are encapsulated in nanocarriers (such as liposomes and micelles). The CEST effects of **Tm-L1**, **Tm-L2**, and **Tm-L3** are linearly dependent on pH and temperature, making them good candidates for dual BIRDS and CEST imaging, as suggested in our previous study.[16] The pH-sensitive CEST profiles of **Tm-L1** and **Tm-L2** can be used for pH-contrasted imaging, while the temperature readouts could be provided by BIRDS. Overall, based on solubility and BIRDS/CEST performances, **Tm-L2** is the best candidate for future in vivo work.

3.6 | In vitro temperature mapping with BIRDS and *Z* spectra with CEST

We used samples containing 4 mM of each of **Tm-L1**, **Tm-L2**, and **Tm-L3** to demonstrate the capability of each agent to generate temperature mapping with BIRDS and *Z* spectra with CEST (Figure 6). It should be noted that both **Tm-L1** and **Tm-L2** could dissolve in water at 10 mM concentration. Thus, the agents' solubilities are at least 4mM for **Tm-L3**, and at least 10 mM for **Tm-L1** and **Tm-L2**. Regardless, the in vitro data shown in Figure 6 feature the high BIRDS/CEST imaging sensitivities of these agents.

We obtained BIRDS datasets in 6 min at 1 μL spatial resolution ($1 \times 1 \times 1$ mm^3 voxel size) for each agent using 3D MRSI and we calculated the corresponding temperature maps using the chemical shifts of methyl group resonances according to Equation 3 and Table 2. For **Tm-L1** we used the difference between the $CH_3^{2,3}$ and the bulk water resonances (Figure 6A), for **Tm-L2** the difference between $CH_3^{2,3}$ and CH_3^{1} resonances (Figure 6B), and for **Tm-L3** the difference between CH_3^{2} and CH_3^{1} resonances (Figure 6C). Since each of these samples was measured separately, the average temperature was different for each: 26.1 ± 0.5 °C for **Tm-L1**, 24.7 ± 0.3 °C for **Tm-L2**, and 23.8 ± 0.2 °C for **Tm-L3**

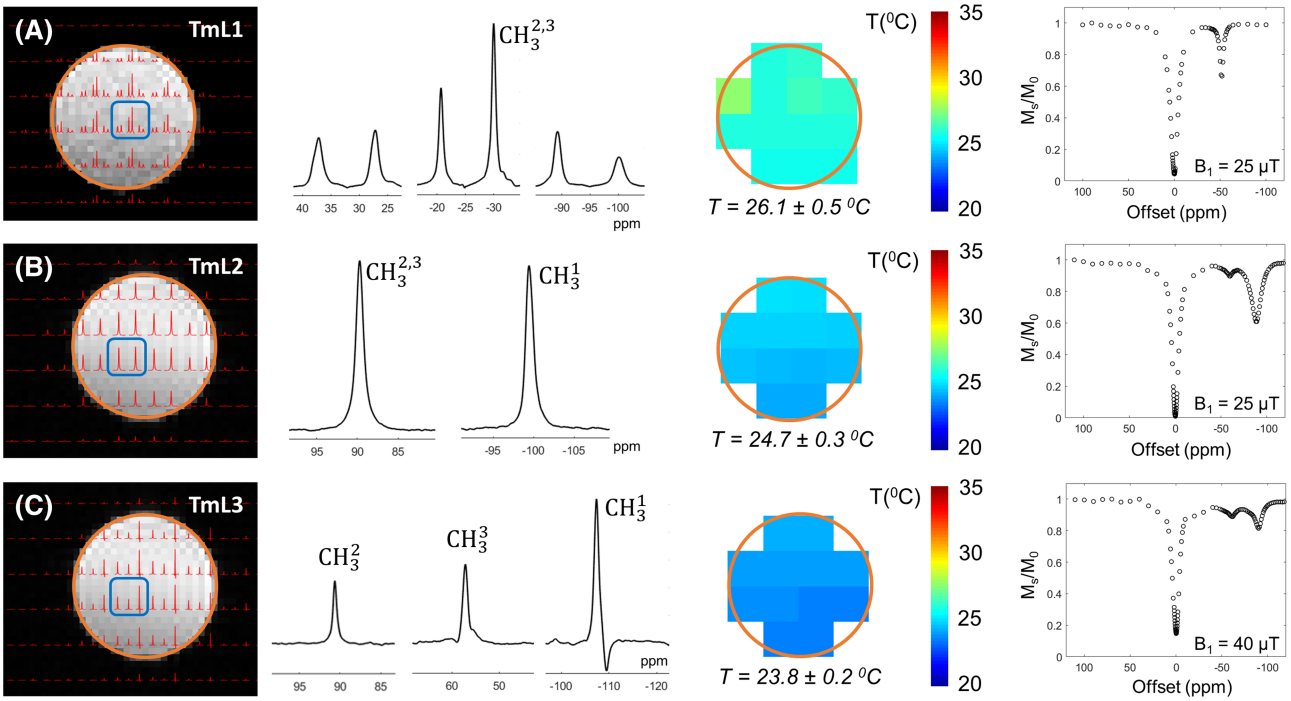

FIGURE 6 Temperature mapping with BIRDS and corresponding *Z* spectra for CEST in samples of **Tm-L1** (A), **Tm-L2** (B), and **Tm-L3** (C). Each sample had a concentration of 4 mM. The temperature was calculated using the chemical shifts of methyl groups indicated for each agent according to Equation 3 and Table 2. The negative component at −108 ppm in the MR spectrum for **Tm-L3** corresponds to the exchangeable amide proton, which partially overlaps with the CH_3^1 methyl resonance but has a different phase due to its fast exchange with the bulk water. The CEST datasets were obtained with a B_1 of 25 μT for **Tm-L1** and **Tm-L2**, while for **Tm-L3** a higher B_1 of 40 μT was used, to enhance the CEST signal of exchangeable peaks

(Figure 6). The temperature variation observed in these experiments most likely reflects the temperature variation inside the magnet bore and the relatively long duration required for temperature equilibration between the sample and its environment. BIRDS-based pH mapping with these agents is not feasible because the chemical shifts of their methyl resonances are not pH dependent in the pH range 6 to 8 observed for in vivo measurements in tumors or normal tissue. Regardless, the coalesced signals of methyl groups in each complex provide high BIRDS sensitivity for molecular imaging.

To demonstrate the feasibility of using these agents for various CEST applications, we obtained average *Z* spectra (see Section 2) in the same experimental sessions for each of the **Tm-L1**, **Tm-L2**, and **Tm-L3** agents (Figure 6, right). The CEST datasets were obtained with a B_1 of 25 μT for **Tm-L1** and **Tm-L2**, while for **Tm-L3** a higher B_1 (40 μT) was used to enhance and better visualize the CEST signal of exchangeable peaks. The differences between the CEST signal amplitudes in the *Z* spectra shown in Figure 5 and those in Figure 6 is due to different sample temperatures (35 °C in Figure 5, 23-26 °C in Figure 6) which affects the chemical exchange rate of exchangeable protons.

4 | CONCLUSIONS

In this work we introduce three heavily methylated tetra-amide Tm^{3+} complexes for absolute temperature/pH mapping with BIRDS and CEST. While variations in structure are subtle between the complexes, the impact on biosensing is actually quite large because of where the methyl groups are located in relation to the metal center (i.e., both proximal and distal). Thus, the temperature and pH sensitivities from BIRDS and CEST, respectively, are quite impressive. While **Tm-L3** is an excellent temperature sensor with sensitivity of −1.93 ppm/°C and quite high SNR for BIRDS (i.e., T_2/T_1 ratio of ∼0.8), it has low CEST performance. However, it seems that **Tm-L2** has a similar temperature sensitivity to $TmDOTMA^-$ (i.e., −0.74 ppm/°C) but much higher SNR for BIRDS (i.e., T_2/T_1 ratio of ∼0.9) and it has high CEST contrast, similar to previously reported lanthanide agents with slow exchange rates that have linear pH dependence. Based on the in vitro molecular imaging results for **Tm-L2**, which has two visible CEST peaks and prominent BIRDS features, we expect that this probe would be a good candidate for BIRDS/CEST hybrid imaging. In the future, temperature mapping with BIRDS using these complexes can be employed to determine the saturation frequency offset for CEST imaging and to correct the temperature induced effects to provide more accurate pH mapping with CEST.

ACKNOWLEDGEMENT

This work was supported by the R01-EB023366 and R01-CA140102 grants from the National Institutes of Health.

CONFLICTS OF INTEREST

Federico A. Rojas-Quijano, Paul Jurek and Garry E Kiefer are employees of Macrocyclics (Dallas, Texas). All the other authors declare no conflicts of interest.

ORCID

Abul B. M. Zakaria https://orcid.org/0000-0001-9329-0163
Daniel Coman https://orcid.org/0000-0002-6289-0817
Sandeep K. Mishra https://orcid.org/0000-0002-1016-0206

REFERENCES

1. Herborn CU, Honold E, Wolf M, et al. Clinical safety and diagnostic value of the gadolinium chelate gadoterate meglumine (Gd-DOTA). *Invest Radiol*. 2007;42(1):58-62.
2. Kubicek V, Toth E. Design and function of metal complexes as contrast agents in MRI. *Adv Inorg Chem*. 2009;61:63-129.
3. Bonnet CS, Toth E. Smart MR imaging agents relevant to potential neurologic applications. *Am J Neuroradiol*. 2010;31(3):401-409.
4. Zuo CS, Mahmood A, Sherry AD. $TmDOTA^{-}$: a sensitive probe for MR thermometry in vivo. *J Magn Reson*. 2001;151(1):101-106.
5. Hekmatyar SK, Poptani H, Babsky A, Leeper DB, Bansal N. Non-invasive magnetic resonance thermometry using thulium-1,-4,7,10-tetraazacyclododecane-1,4,7,10-tetraacetate (TmDOTA-). *Int J Hyperthermia*. 2002;18:(3):165-179. https://doi.org/10.1080/02656730110098598
6. Coman D, Trubel HK, Hyder F. Brain temperature by Biosensor Imaging of Redundant Deviation in Shifts (BIRDS): Comparison between TmDOTP5− and TmDOTMA−. *NMR Biomed*. 2010;23:(3):277-285. https://doi.org/10.1002/nbm.1461
7. Bleaney B. Nuclear magnetic resonance shifts in solution due to lanthanide ions. *J Magn Reson*. 1972;8(1):91-100.
8. Harnden AC, Parker D, Rogers NJ. Employing paramagnetic shift for responsive MRI probes. *Coord Chem Rev*. 2019;383:30-42. https://doi.org/10.1016/j.ccr.2018.12.012
9. Soesbe TC, Wu Y, Sherry AD. Advantages of paramagnetic chemical exchange saturation transfer (CEST) complexes having slow to intermediate water exchange properties as responsive MRI agents. *NMR Biomed*. 2013;26(7):829-838.
10. Hancu I, Dixon WT, Woods M, Vinogradov E, Sherry AD, Lenkinski RE. CEST and PARACEST MR contrast agents. *Acta Radiol*. 2010;51(8):910-923.
11. Coman D, Trubel HK, Rycyna RE, Hyder F. Brain temperature and pH measured by1H chemical shift imaging of a thulium agent. *NMR Biomed*. 2009;22:(2):229-239. https://doi.org/10.1002/nbm.1312
12. Trubel HK, Maciejewski PK, Farber JH, Hyder F. Brain temperature measured by ^{1}H-NMR in conjunction with a lanthanide complex. *J Appl Physiol*. 2003;94(4):1641-1649.
13. Zhang X, Yuan Y, Li S, et al. Free-base porphyrins as CEST MRI contrast agents with highly upfield shifted labile protons. *Magn Reson Med*. 2019;82(2):577-585.
14. Yang X, Song X, Li Y, et al. Salicylic acid and analogues as diaCEST MRI contrast agents with highly shifted exchangeable proton frequencies. *Angew Chem*. 2013;125(31):8274-8277.
15. Coman D, Kiefer GE, Rothman DL, Sherry AD, Hyder F. A lanthanide complex with dual biosensing properties: CEST (chemical exchange saturation transfer) and BIRDS (biosensor imaging of redundant deviation in shifts) with europium DOTA-tetraglycinate. *NMR Biomed*. 2011;24(10):1216-1225.
16. Huang Y, Coman D, Ali MM, Hyder F. Lanthanide ion (III) complexes of 1,4,7,10-tetraazacyclododecane-1,4,7,10-tetraaminophosphonate for dual biosensing of pH with chemical exchange saturation transfer (CEST) and biosensor imaging of redundant deviation in shifts (BIRDS). *Contrast Media Mol Imaging*. 2014;10(1):51-58.
17. Sherry AD, Wu Y. The importance of water exchange rates in the design of responsive agents for MRI. *Curr Opin Chem Biol*. 2013;17(2):167-174.
18. Walsh JJ, Huang Y, Simmons JW, et al. Dynamic thermal mapping of localized therapeutic hypothermia in the brain. *J Neurotrauma*. 2020;37(1):55-65.
19. Coman D, Sanganahalli BG, Jiang L, Hyder F, Behar KL. Distribution of temperature changes and neurovascular coupling in rat brain following 3,4-methylenedioxymethamphetamine (MDMA, "ecstasy") exposure. *NMR Biomed*. 2015;28:(10):1257-1266. https://doi.org/10.1002/nbm.3375
20. Delli Castelli D, Ferrauto G, Cutrin JC, Terreno E, Aime S. In vivo maps of extracellular pH in murine melanoma by CEST-MRI. *Magn Reson Med*. 2014;71(1):326-332.
21. Delli Castelli D, Terreno E, Aime S. YbIII-HPDO3A: A dual pH- and temperature-responsive CEST agent. *Angew Chemie Int Ed Engl*. 2011;50(8):1798-1800. https://doi.org/10.1002/anie.201007105
22. Coman D, Huang Y, Rao JU, et al. Imaging the intratumoral-peritumoral extracellular pH gradient of gliomas. *NMR Biomed*. 2016;29(3):309-319.
23. Huang Y, Coman D, Herman P, Rao JU, Maritim S, Hyder F. Towards longitudinal mapping of extracellular pH in gliomas. *NMR Biomed*. 2016;29(10):1364-1372.
24. Rao JU, Coman D, Walsh JJ, Ali MM, Huang Y, Hyder F. Temozolomide arrests glioma growth and normalizes intratumoral extracellular pH. *Sci Rep*. 2017;7:7865.
25. Walsh JJ, Parent M, Akif A, et al. Imaging hallmarks of the tumor microenvironment in glioblastoma progression. *Frontiers in Oncology*. 2021;11:692650. https://doi.org/10.3389/fonc.2021.692650
26. Coman D, Peters DC, Walsh JJ, et al. Extracellular pH mapping of liver cancer on a clinical 3T MRI scanner. *Magn Reson Med*. 2020;83(5):1553-1564.
27. Savic LJ, Schobert IT, Peters D, et al. Molecular imaging of extracellular tumor pH to reveal effects of locoregional therapy on liver cancer microenvironment. *Clin Cancer Res*. 2020;26(2):428-438.

28. Mihailovic JM, Huang Y, Walsh JJ. High-resolution pH imaging using ratiometric chemical exchange saturation transfer combined with biosensor imaging of redundant deviation in shifts featuring paramagnetic DOTA-tetraglycinate agents. *NMR Biomed*. 2021:1-15. https://doi.org/10.1002/nbm.4658
29. Ratnakar SJ, Chirayil S, Funk AM, et al. A frequency-selective pH-responsive paraCEST agent. *Angew Chem Int Ed Engl*. 2020;59(48):21671-21676.
30. Basal LA, Yan Y, Shen Y, Haacke EM, Mehrmohammadi M, Allen MJ. Oxidation-responsive, Eu (II/III)-based, multimodal contrast agent for magnetic resonance and photoacoustic imaging. *ACS Omega*. 2017;2(3):800-805.
31. Mani T, Tircsó G, Togao O, et al. Modulation of water exchange in Eu(III) DOTAhyphentetraamide complexes: Considerations forin vivoimaging of PARACEST agents. *Contrast Media Mol Imaging*. 2009;4(4):183-191. https://doi.org/10.1002/cmmi.279
32. Sheldrick GM. Crystal structure refinement with SHELXL. *Acta Crystallogr C*. 2015;71(1):3-8.
33. Rappe AK, Casewit CJ, Colwell KS, Goddard WA, Skiff WM. UFF, a full periodic table force field for molecular mechanics and molecular dynamics simulations. *J Am Chem Soc*. 1992;114(25):10024-10035. https://doi.org/10.1021/ja00051a040
34. Woessner DE, Zhang S, Merritt ME, Sherry AD. Numerical solution of the Bloch equations provides insights into the optimum design of PARACEST agents for MRI. *Magn Reson Med*. 2005;53(4):790-799.
35. Hekmatyar SK, Hopewell P, Pakin SK, Babsky A, Bansal N. Noninvasive MR thermometry using paramagnetic lanthanide complexes of 1,4,7,10-tetraazacyclododecane-α,α′,α″,α‴-tetramethyl-1,4,7,10- tetraacetic acid ($DOTMA^{4-}$). *Magn Reson Med*. 2005;53(2):294-303.
36. Aime S, Botta M, Ermondi G. NMR study of solution structures and dynamics of lanthanide (III) complexes of DOTA. *Inorg Chem*. 1992;31(21):4291-4299.
37. Mason K, Rogers NJ, Suturina EA, et al. PARASHIFT probes: solution NMR and X-ray structural studies of macrocyclic ytterbium and yttrium complexes. *Inorg Chem*. 2017;56(7):4028-4038.
38. Woods M, Aime S, Botta M. Correlation of water exchange rate with isomeric composition in diastereoisomeric gadolinium complexes of tetra(carboxyethyl)dota and related macrocyclic ligands. *J Am Chem Soc*. 2000;122:(40):9781-9792. https://doi.org/10.1021/ja994492v
39. Howard JAK, Kenwright AM, Moloney JM, et al. Structure and dynamics of all of the stereoisomers of europium complexes of tetra (carboxyethyl) derivatives of dota: ring inversion is decoupled from cooperative arm rotation in the *RRRR* and *RRRS* isomers. *Chem Commun*. 1998;(13):1381-1382.
40. Woods M, Kovacs Z, Kiraly R, Brücher E, Zhang S, Sherry AD. Solution dynamics and stability of lanthanide (III)(S)-2-(p-nitrobenzyl) DOTA complexes. *Inorg Chem*. 2004;43(9):2845-2851.
41. Di Bari L, Pintacuda G, Salvadori P. Stereochemistry and near-infrared circular dichroism of a chiral Yb complex. *J Am Chem Soc*. 2000;122(23):5557-5562.
42. Aime S, Botta M, Garda Z, et al. Properties, solution state behavior, and crystal structures of chelates of DOTMA. *Inorg Chem*. 2011;50(17):7955-7965.
43. Tsitovich PB, Cox JM, Benedict JB, Morrow JR. Six-coordinate iron (II) and cobalt (II) paraSHIFT agents for measuring temperature by magnetic resonance spectroscopy. *Inorg Chem*. 2016;55(2):700-716.
44. Ren J, Zhang S, Dean Sherry A, Geraldes CFGC. Analysis of lanthanide induced NMR shifts using a crystal field independent method: application to complexes of tetraazamacrocyclic ligands. *Inorg Chim Acta*. 2002;339:273-282.
45. Peters JA, Huskens J, Raber DJ. Lanthanide induced shifts and relaxation rate enhancements. *Prog Nucl Magn Reson Spectrosc*. 1996;28(3):283-350.
46. Coman D, de Graaf RA, Rothman DL, Hyder F. In vivo three-dimensional molecular imaging with Biosensor Imaging of Redundant Deviation in Shifts (BIRDS) at high spatiotemporal resolution. *NMR Biomed*. 2013;26(11):1589-1595.
47. Harvey P, Blamire AM, Wilson JI, et al. Moving the goal posts: enhancing the sensitivity of PARASHIFT proton magnetic resonance imaging and spectroscopy. *Chem Sci*. 2013;4(11):4251-4258.
48. Milne M, Hudson RH. Contrast agents possessing high temperature sensitivity. *Chem Commun*. 2011;47(32):9194-9196.
49. Torchilin VP. Recent advances with liposomes as pharmaceutical carriers. *Nat Rev Drug Discov*. 2005;4(2):145-160.
50. Maritim S, Huang Y, Coman D, Hyder F. Characterization of a lanthanide complex encapsulated with MRI contrast agents into liposomes for biosensor imaging of redundant deviation in shifts (BIRDS). *J Biol Inorg Chem*. 2014;19(8):1385-1398.
51. Zhang S, Wu K, Sherry AD. Unusually sharp dependence of water exchange rate versus lanthanide ionic radii for a series of tetraamide complexes. *J Am Chem Soc*. 2002;124(16):4226-4227.
52. Pubanz D, Gonzalez G, Powell DH, Merbach AE. Unexpectedly large change of water exchange rate and mechanism on [Ln(DTPA-BMA)(H2O)] complexes along the lanthanide(III) series. *Inorg Chem*. 1995;34(17):4447-4453.
53. Aime S, Botta M, Crich SG, et al. NMR relaxometric studies of Gd (III) complexes with heptadentate macrocyclic ligands. *Magn Reson Chem*. 1998;36(S1):S200-S208.
54. Persson I, D'Angelo P, De Panfilis S, Sandström M, Eriksson L. Hydration of lanthanoid(III) ions in aqueous solution and crystalline hydrates studied by EXAFS spectroscopy and crystallography: The myth of the "gadolinium break". *Chem Eur J*. 2008;14(10):3056-3066.
55. Viswanathan S, Kovacs Z, Green KN, Ratnakar SJ, Sherry AD. Alternatives to gadolinium-based metal chelates for magnetic resonance imaging. *Chem Rev*. 2010;110(5):2960-3018.
56. Aime S, Barge A, Delli Castelli D, et al. Paramagnetic lanthanide (III) complexes as pH-sensitive chemical exchange saturation transfer (CEST) contrast agents for MRI applications. *Magn Reson Med*. 2002;47(4):639-648.
57. Zhang S, Malloy CR, Sherry AD. MRI thermometry based on PARACEST agents. *J Am Chem Soc*. 2005;127(50):17572-17573.
58. Zhang S, Trokowski R, Sherry AD. A paramagnetic CEST agent for imaging glucose by MRI. *J Am Chem Soc*. 2003;125(50):15288-15289.
59. Aime S, Delli Castelli D, Fedeli F, Terreno E. A paramagnetic MRI-CEST agent responsive to lactate concentration. *J Am Chem Soc*. 2002;124(32):9364-9365.
60. Trokowski R, Ren J, Kalman FK, Sherry AD. Selective sensing of zinc ions with a PARACEST contrast agent. *Angew Chem Int Ed Engl*. 2005;44(42):6920-6923.
61. Vinogradov E, Sherry AD, Lenkinski RE. CEST: from basic principles to applications, challenges and opportunities. *J Magn Reson*. 2013;229:155-172.
62. Delli Castelli D, Dastrù W, Terreno E, et al. In vivo MRI multicontrast kinetic analysis of the uptake and intracellular trafficking of paramagnetically labeled liposomes. *J Control Release*. 2010;144(3):271-279. https://doi.org/10.1016/j.jconrel.2010.03.005

SUPPORTING INFORMATION

Additional supporting information may be found in the online version of the article at the publisher's website.

How to cite this article: Zakaria ABM, Huang Y, Coman D, et al. Methylated tetra-amide derivatives of paramagnetic complexes for magnetic resonance biosensing with both BIRDS and CEST. *NMR in Biomedicine*. 2022;35(6):e4687. doi:10.1002/nbm.4687